

Cite this: *J. Mater. Chem. A*, 2018, **6**,
11416

Facilitating the charge transfer of ZnMoS₄/CuS p–n heterojunctions through ZnO intercalation for efficient photocatalytic hydrogen generation†

Wei Yang Lim,^a Hao Wu,^a Yee-Fun Lim^b and Ghim Wei Ho^{*abc}

Photocatalysts based on p–n junction heterostructures have demonstrated their ability to enhance the separation of photo-generated charge carriers and promote their lifetimes for photocatalytic hydrogen evolution. However, few reported studies have extended to the optimization of charge carrier dynamics to facilitate favorable kinetics of the target surface reaction for photocatalysis. Herein, a novel ternary chalcogenide photocatalyst ZnMoS₄ is developed with ideal multiple heterojunctions of the ZnMoS₄/ZnO/CuS band structure. Besides synergistically enhancing charge carrier separation, more importantly, the intercalated ZnO layer in the ZnMoS₄/CuS p–n heterojunction induces interfacial band bending that consequently allows kinetically desirable electron migration from ZnMoS₄ across the multi-junction heterostructures, towards the photocatalyst surface for an efficient water reduction reaction. This optimized electrodynamic configuration results in a 97% higher hydrogen evolution rate as compared to a typical unoptimized ZnMoS₄/CuS p–n heterostructure. Essentially, this work offers a band structure engineering strategy for heterostructured photocatalyst design which enables efficient charge carrier dynamics and electrochemical reactivity.

Received 26th March 2018
Accepted 14th May 2018

DOI: 10.1039/c8ta02763c

rsc.li/materials-a

Because of the highly negative potential conduction band and rapid photo-generation of electron–hole pairs, ZnS displays a high versatility in its functions as a photocatalyst, such as photoreduction of CO₂, photocatalytic degradation of organic pollutants, and photocatalytic water splitting in generating H₂.¹ Besides, it also shows other advantages in terms of electronic mobility, nontoxicity and earth abundance.² However, its wide optical band gap feature, high electron–hole recombination and instability in aqueous solution have limited its application.³ Particularly in photocatalytic hydrogen evolution, numerous efforts have been made, in attempts to solve ZnS practical issues. For instance, metal ion doping,^{4,5} nonmetal ion doping,⁶ ZnS solid solution formation^{7,8} and Zn-based ternary chalcogenide development^{9,10} were reported to construct narrower band gap ZnS counterparts, allowing more photon absorption for enhanced water reduction reactions. Surface modification or hybridization of ZnS with a cocatalyst to create heterojunctions and hybrids is well known for enhancing charge transfer and

suppressing recombination for improved photocatalytic efficiency, such as ZnS/CuS, ZnS/g-C₃N₄ and ZnS/ZnO.^{11–13} Several attempts were also made to solve the ZnS photostability issue through mitigation and encapsulation design.^{14,15} Nevertheless, in regard to these achievements in tackling respective issues, it is clear that each individual approach could not yield all the required features to overcome the diverse issues synchronously. Hence, it is essential to strategically integrate multiple components through the construction of synergic interface and heterostructure architectures that are mutually beneficial for photocatalytic performances.^{16,17}

Furthermore, in pursuit for better photocatalytic hydrogen evolution properties in many n-type photocatalysts such as TiO₂, ZnS and CdS, various researchers have focused on modifying or compositing the photocatalyst surface with p-type compounds to form heterostructure schemes.^{12,18,19} The strong internal electric field present at the p–n heterojunction interface enables the transfer of opposite charges towards either side of the structure, achieving efficient electron–hole separation.¹⁷ Although it is noted that photocatalysis is a surface-dominated redox reaction, a very few reports have included the optimization of charge carrier dynamics to further facilitate photocatalytic kinetics beyond charge separation. Specifically, in a typical hydrogen evolution photocatalyst configuration where an n-type photocatalyst host is loaded with a p-type cocatalyst on the surface, the photo-generated electrons, which contribute to the reduction reaction, are driven to the n-type host

^aDepartment of Electrical and Computer Engineering, National University of Singapore, 4 Engineering Drive 3, Singapore 117583, Singapore. E-mail: elehgw@nus.edu.sg

^bInstitute of Materials Research and Engineering, A*STAR (Agency for Science, Technology and Research), 2 Fusionopolis Way, Singapore 138634, Singapore

^cEngineering Science Programme, National University of Singapore, 9 Engineering Drive 1, Singapore 117575, Singapore

† Electronic supplementary information (ESI) available. See DOI: 10.1039/c8ta02763c

photocatalyst beneath the interface, while the holes migrate to the p-type cocatalyst at the exterior for the subsequent oxidation reaction. In other words, this commonly adopted heterostructure design may not be the most ideal structure for photocatalytic hydrogen evolution as it does not facilitate electron flow towards the surface reaction sites. Therefore, it is crucial to develop a photocatalyst heterostructure that not only induces electron-hole separation, but also promotes the electron flow kinetics that is constructive towards photocatalytic water reduction.

Herein, a novel ternary Zn-based p-n heterostructured photocatalyst, $\text{ZnMoS}_4/\text{ZnO}/\text{CuS}$, with a 2D hexagonal plate microstructure is designed to enhance surface mediated photocatalytic hydrogen evolution. Unlike the conventional p-n heterojunction design, a kinetically optimized charge carrier dynamics is devised for the $\text{ZnMoS}_4/\text{CuS}$ p-n heterojunction by forming a layer of ZnO between ZnMoS_4 and CuS, to realize the $\text{ZnMoS}_4/\text{ZnO}/\text{CuS}$ scheme. Explicitly, the ZnO interface generates an interfacial band bending that significantly lowers the Fermi level of ZnMoS_4 , such that upon contact with CuS, the p-n heterojunction band shifting is minimal. This results in a switch of charge carrier dynamics in a way that instead of facilitating hole transfer, it favors a smooth electron flow across multiple heterojunction interfaces to the photocatalyst surface for an efficient water reduction reaction. This work highlights a strategic band structure engineering technique to enable charge transfer dynamics for electrochemical reactions, which has not been demonstrated before.

The synthesis processes of zinc molybdenum compounds are summarized in Fig. 1a. As shown in Fig. 1b and c, $\text{Zn}_5\text{Mo}_2\text{O}_{11}$ and ZnMoS_4 with 5–8 μm in size and 500 nm in thickness were synthesized. The 2D hexagonal plate microstructures are preserved through the sulfidation process, suggesting that $\text{Zn}_5\text{Mo}_2\text{O}_{11} \cdot 5\text{H}_2\text{O}$ partakes in the sulfidation process as both a Zn and Mo chemical composition source and a 2D microstructure template. However, it can also be observed that the sulfidised plate shows voids and a roughened surface, indicating the formation of pores during the sulfidation process. This observation is in agreement with the reported literature, likely due to the Kirkendall effect originating from the difference in the ionic radius between O (1.40 Å) and S (1.84 Å), and their corresponding diffusion rates.^{20–23} An annealing process under ambient atmosphere at 500 °C was

then carried out to introduce an oxide layer onto the surface of the ZnMoS_4 plate. The temperature of 500 °C was chosen to control the occurrence of the oxidation exclusively on the surface, or else, bulk diffusion of oxygen species will occur and transform the whole structure into an oxide at a temperature beyond 500 °C, as reported in numerous studies.^{24–26} The microstructure of the annealed product is shown in Fig. 1d. It can be clearly seen that the annealing process and the introduction of the oxide layer have visibly changed the microstructure, as the hexagonal plate size and its rough surface appear similar to those of ZnMoS_4 in Fig. 1c.

Further characterization was employed to investigate all three ZnMo compounds produced from the three respective synthesis steps. Their XRD diffraction spectra are plotted in Fig. 2a. The formation of the $\text{Zn}_5\text{Mo}_2\text{O}_{11}$ 2D hexagonal plate can be verified from its diffraction pattern, in agreement with the index of PDF#30-1486. The diffraction pattern of ZnMoS_4 is in line with the reported literature, with no signal from other derivatives or compounds being observed, indicating a complete sulfide transformation.^{27,28} On top of this, upon annealing of ZnMoS_4 in air, its sulfide peaks remain intact, indicating the preservation of ZnMoS_4 throughout the entire annealing process, while a few new small peaks evolved around 30–40°. The peaks can be assigned to the wurtzite ZnO phase, indicating the formation of a ZnO layer resulting from the annealing process. Moreover, Brunauer–Emmett–Teller (BET) measurements were used to quantify the pore and surface area associated with the chemical transformations, where the N_2 adsorption–desorption isotherms and pore size distribution are plotted in Fig. 2b and c respectively. The $\text{Zn}_5\text{Mo}_2\text{O}_{11}$ exhibits a type II characteristic isotherm, which typically represents a non-porous or microporous material. It shows a limited surface area of $6.5 \text{ m}^2 \text{ g}^{-1}$, and a tight pore size distribution with a pore volume of 0.01 mL g^{-1} . On the other hand, ZnMoS_4 exhibits a type IV H3 hysteresis loop with a wide pore size distribution. Its surface area and pore volume increased to $72.7 \text{ m}^2 \text{ g}^{-1}$ and 0.173 mL g^{-1} respectively, distinctly indicating the presence of slit-shaped mesopores resulting from the



Fig. 1 (a) Schematic illustration of ZnMo compound synthesis. Low magnification SEM images of (b) $\text{Zn}_5\text{Mo}_2\text{O}_{11}$, (c) ZnMoS_4 and (d) $\text{ZnMoS}_4/\text{ZnO}$, and the insets show their high magnification SEM images, respectively.

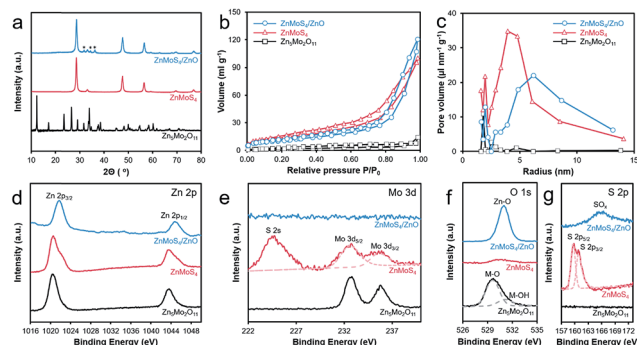


Fig. 2 (a) X-ray diffraction, (b) N_2 adsorption–desorption isotherms measured at 77 K, (c) pore size distribution obtained using the Barrett–Joyner–Halenda (BJH) method, (d) Zn 2p XPS spectra, (e) Mo 3d XPS spectra, (f) O 1s spectra and (g) S 2p XPS spectra of all three ZnMo compounds: $\text{Zn}_5\text{Mo}_2\text{O}_{11}$ (black), ZnMoS_4 (red) and $\text{ZnMoS}_4/\text{ZnO}$ (blue), respectively.

sulfidation process. Likewise, the N_2 adsorption-desorption isotherm of $ZnMoS_4/ZnO$ exhibits a similar hysteresis loop to the $ZnMoS_4$, the pore size distribution remains comparably wide and the pore volume remains at 0.156 mL g^{-1} , but its surface area is reduced to $38.7 \text{ m}^2 \text{ g}^{-1}$. It is believed that this might be due to the smoothing of surface roughness associated with the formation of the ZnO layer on the hexagonal plate and pore surface. Nonetheless, the results of surface and pore distribution fairly concur with the SEM results.

In addition, surface composition analyses of the three different ZnMo compounds were performed using X-ray photoelectron spectra (XPS). The spectra of Zn, Mo, O and S are shown in Fig. 2d–g, respectively. The Zn XPS spectrum in Fig. 2d shows that the Zn $2p_{1/2}$ and $2p_{3/2}$ peaks of $Zn_2Mo_5O_{11}$ are located at 1020.7 eV and 1044 eV, while its Mo XPS spectrum in Fig. 2e exhibits the peaks of Mo $3d_{3/2}$ and $3d_{5/2}$ at 232.6 eV and 235.8 eV, respectively, indicative of the presence of typical Zn^{2+} and Mo^{6+} ions.^{3,29,30} The 529.6 eV and 534.1 eV peaks of the O 1s spectrum in Fig. 2f can be mapped to the corresponding metal-oxygen bonds and hydroxyl species,^{31,32} confirming the synthesis of $Zn_5Mo_2O_{11} \cdot 5H_2O$. After the sulfidation step, Fig. 2e shows the retention of the Mo^{6+} characteristic 3d peaks. A complete sulfidation into sulfide $ZnMoS_4$ is verified by the disappearance of the O 1s peak and the concurrent emergence of S 2p doublets in Fig. 2f and g. In the annealed product, it is noted that the peak position of Zn^{2+} in $ZnMoS_4/ZnO$ differs from that in $ZnMoS_4$, as the presence of ZnO results in peak-shifting towards higher binding energy, consistent with other reports.¹⁵ The S 2p doublets in Fig. 2g disappear, and a weak broad peak appears at 166 eV, which corresponds to the sulfate species SO_x .^{33,34} In addition, an intensified O 1s peak (Fig. 2f) can be observed. These findings collectively indicate that the sulfide is oxidized, confirming the formation of a thin oxide layer on the surface of $ZnMoS_4$. With no Mo peak being detected in the annealed product, it can be verified that the surface does not contain any Mo–S derivatives, but rather a layer of ZnO several nanometers in thickness. Hence, together with the XRD results, it can be deduced that the sulfidation process has fully transformed $Zn_5Mo_2O_{11}$ into $ZnMoS_4$, while the subsequent annealing process in air turned the surface of $ZnMoS_4$ into ZnO.

Transmission electron microscopy (TEM) was used to further assess 2D hexagonal plate compositional and structural information. Fig. 3a shows the $ZnMoS_4$ 2D hexagonal plate at low magnification. The $ZnMoS_4$ plate appears to be rough and porous, strikingly in contrast to the smooth and non-porous $Zn_5Mo_2O_{11}$ as shown in Fig. S1a.† This complies with the SEM observations as well as the N_2 adsorption-desorption and pore size distribution results. Upon closer observation, it is found that the hexagonal plate consists of cluster-like nanoparticles (nanocrystallites) of less than 20 nm. Clearly, the nanoparticles contribute to the porosity as seen in the sulfurized ZnMo compound, owing to the Kirkendall effect from the sulfidation step.²² Nonetheless, the high surface areas and pores can lead to increased surface catalytic reaction sites. In the high resolution TEM image in Fig. 3c, the porous plate can be identified as $ZnMoS_4$ from the d -spacing of 0.31 nm. Moreover, the nanoparticle feature is unaltered after the annealing step, as

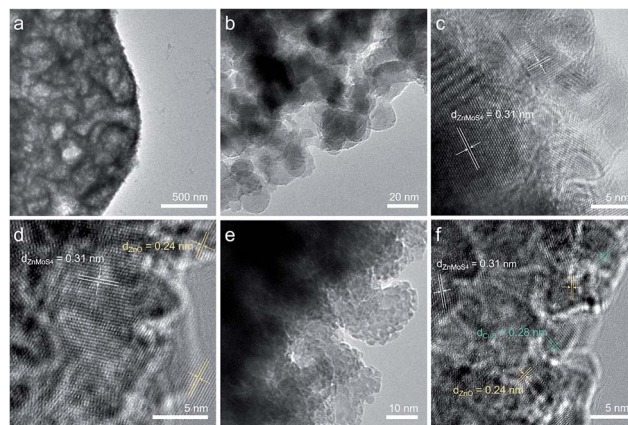


Fig. 3 (a and b) TEM images and (c) HRTEM image of $ZnMoS_4$; (d) HRTEM image of $ZnMoS_4/ZnO$; and (e) TEM image and (f) HRTEM of $ZnMoS_4/ZnO/CuS$. d -spacing 0.31 nm, 0.24 nm and 0.28 nm correspond to $ZnMoS_4$, ZnO and CuS, respectively.

presented in Fig. S1b,† indicating that the air annealing is a structurally non-destructive process. Furthermore, lattice fringes of 0.24 nm d -spacing are detected at the outer surface of the particles, which can be identified as ZnO, verifying the growth of a ZnO layer of ~ 5 nm after the annealing process, complementary to XPS analysis. Notably, due to the high degree of porosity, the formation of ZnO can occur all over its nanostructural interior, not limited to the microstructural basal plane or outer plane edge. Essentially, the entire hexagonal plate composition is a hybrid of $ZnMoS_4$ and ZnO, with the ZnO predominantly present at the outer surface.

CuS was loaded successively onto $ZnMoS_4/ZnO$ through a photodeposition method, according to a method previously reported.³⁵ The photo-deposited $ZnMoS_4/ZnO/CuS$ shows microstructures that are indistinguishable from its precedents, preserving the original hexagonal plate structure (Fig. S2a†). CuS loading can be identified under TEM, as shown in Fig. 3e and f, as fine particles (< 5 nm) that are well-dispersed at the outer surfaces of the nanoparticles. Fig. S2b† shows that both CuS loaded samples, namely $ZnMoS_4/CuS$ and $ZnMoS_4/ZnO/CuS$, display the same diffraction feature, *i.e.* a weak broad peak at around 31.8° . This peak is consistent with the CuS peak maximum for the (103) plane. The weak peak suggests a low quantity of CuS loading, while the broad peak affirms the formation of fine CuS crystallites (< 5 nm).³⁶ Moreover, the CuS nanoparticles are validated by the clear lattice fringes of 0.28 nm d -spacing (Fig. S2c†). In brief, with two consecutive surface modifications on $ZnMoS_4$: first, post-annealing step to oxidize the sulfide surface into ZnO; and second, photo-deposition step to introduce CuS nanoparticles, $ZnMoS_4/ZnO/CuS$ structure is created (Fig. 3f). Lattice fringes with three different interplanar spacings can be found altogether, *i.e.* 0.31 nm, 0.24 nm and 0.28 nm that correspond to $ZnMoS_4$, ZnO and CuS, respectively.

The photocatalytic properties of ZnS have been widely reported, and in contrast, $ZnMoS_4$ caught very little attention. From the fact that $ZnMoS_4$ and ZnS comprise the same crystal

structure,^{37,38} as shown in Fig. S3a,† a study on the role of Mo in the photocatalysis becomes methodically accessible. To effectively examine the compositional factor, ZnS with the same 2D hexagonal plate microstructure was synthesized under similar two-step aqueous heating, such that it could mimic the phase transformation step of ZnMoS₄. Specifically, ZnO hexagonal plates with a similar lateral size of 5–8 μm and little thinner in thickness (30 nm) were constructed and subsequently subjected to sulfidation to transform into surface-roughened ZnS. The SEM images of the ZnO and ZnS 2D hexagonal plates are displayed in Fig. S3c and d.† It is noted that since both ZnMoS₄ and ZnS have a similar shape and dimensions, the contribution towards photocatalytic performance from these physical factors can be excluded, thereby, favourably narrowing the analysis on the effect of Mo composition down to its electronic properties. Fig. 4a shows the Mott–Schottky plot (M–S plot) of ZnMoS₄ and ZnS, in accordance with the following equation:³⁹

$$\frac{1}{C^2} = \frac{2}{\varepsilon\varepsilon_0eN_D} \left(E - E_{fb} - \frac{k_B T}{e} \right) \quad (1)$$

where C is the space charge capacitance obtained from electrochemical impedance spectra (EIS), ε and ε_0 are the dielectric constant of the semiconductor and permittivity in vacuum, e is the electronic charge, and N_D is the charge carrier density, respectively. Alternatively, the charge carrier density N_D can be derived from the following equation:¹⁷

$$N_D = \frac{2}{\varepsilon\varepsilon_0e} \frac{dE}{d\frac{1}{C^2}} = \frac{2}{\varepsilon\varepsilon_0e} \frac{1}{\text{slope}} \quad (2)$$

where slope is the slope of the M–S plot. In other words, the M–S plot can be utilized to extract flat band potential regarding the photocatalyst/electrolyte interface (eqn (1)), and charge carrier density from its slope (eqn (2)).

The M–S plot in Fig. 4a reveals that both ZnMoS₄ and ZnS primarily exhibit positive M–S plot slopes, featuring n-type semiconductors. The plots were extrapolated to $1/C^2 = 0$ to project the value of E_{fb} from eqn (1), giving -0.66 V and -0.62 V for ZnS and ZnMoS₄, respectively. It indicates an approximately 40 mV positive shift of the flat band potential, which corresponds to a decrease in bending of the band edge, and therefore promotes interfacial charge transfer.^{40,41} It is also observed that ZnMoS₄ has a gentler slope than that of ZnS, representing higher charge carrier density as compared to bare ZnS, based on

eqn (2). In contrast to ZnS, a negative slope in the M–S plot is found in the potential range of <0.75 V vs. SCE, in the case of ZnMoS₄. This suggests a co-existence of both n-type and p-type conductivities and signifies a p-type defect state resulting from the inclusion of Mo species. This p-type defect state forms a new donor level in the valence band and possibly contributes additional photo-generated electrons.^{42,43} Consequently, from UV-visible spectroscopy measurements, it is found that ZnMoS₄ shows higher photoabsorbance than ZnS, *i.e.* in the UV light region (<420 nm), as depicted in the inset of Fig. S3b.† This result is attributed to the additional donor level and higher intrinsic carrier density, which enables ZnMoS₄ to have improved photo-activated capabilities, thereby absorbing more photons and resulting in higher photo-generated charge carriers. Furthermore, the Tauc gap was calculated to estimate the band gaps of ZnS and ZnMoS₄.^{35,44} Their Tauc plots are outlined (Fig. S3b†), and by extrapolating their linear regime to an abscissa, the optical band gap E_g of ZnS and ZnMoS₄ is determined to be 3.52 eV and 3.35 eV,^{44,45} respectively. It is believed that the narrower band gap in ZnMoS₄ is caused by the new donor level. Collectively, through isolating their electronic contribution, it is illustrated that the incorporation of Mo species reinforces efficient interfacial charge dynamics due to its reduced Schottky barrier, higher intrinsic charge carrier density, and increased photo-activated charge carriers originated from the defect state. Accordingly, the photocatalytic hydrogen generation of both photocatalysts using a 365 nm UV LED was examined and is plotted in Fig. 4b. ZnS and ZnMoS₄ show hydrogen evolution rates of 1.53 mmol g⁻¹ h⁻¹ and 5.79 mmol g⁻¹ h⁻¹, respectively, corresponding to a 3.78-fold enhancement in photocatalytic activity. Apparently, this outcome can be attributed to the electronic features brought about by the Mo counterpart, demonstrating the competency of ZnMoS₄ as a hydrogen evolution photocatalyst.

To further enhance its photocatalytic potential, ZnMoS₄ was loaded with the CuS co-catalyst to form a heterojunction for improved charge separation. CuS is loaded *via* a photo-deposition method according to a previous report.³⁵ The photocatalytic H₂ generation performances of ZnMoS₄ loaded with various amounts of CuS were plotted (Fig. S4† and 5a). It is demonstrated that with increasing amount of CuS loading, the photocatalytic hydrogen production rates are enhanced. The greatest enhancement was observed at 1 wt% CuS loading, with ZnMoS₄/1 wt% CuS producing a hydrogen evolution rate of 19.38 mmol g⁻¹ h⁻¹, equivalent to a 235% boost in photocatalytic performance compared to 5.79 mmol g⁻¹ h⁻¹ in bare ZnMoS₄. However, excessive addition of CuS beyond 1 wt% results in a decline in the photocatalytic performances. The overloading of the surface cocatalyst will lead to active site screening and light absorption shielding of the host photocatalyst, which was proven to be detrimental to photocatalytic activities.^{35,46} Prominently, this report focuses on the introduction of a thin ZnO intercalated layer into a heterojunction to further improve charge carrier dynamics. As mentioned earlier, a ZnO layer was created through air annealing the ZnMoS₄ host photocatalyst prior to photo-deposition of CuS. The impact of ZnO in promoting photocatalytic H₂ evolution performance is

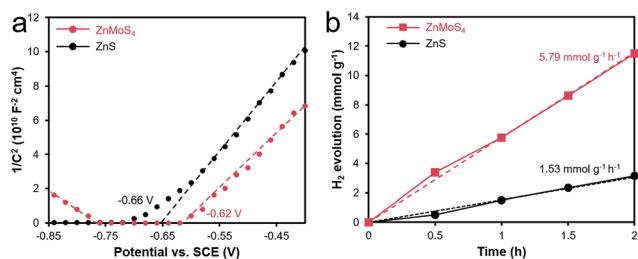


Fig. 4 (a) Mott–Schottky plots and (b) photocatalytic hydrogen evolution versus time plot of ZnS and ZnMoS₄ under UV LED illumination.

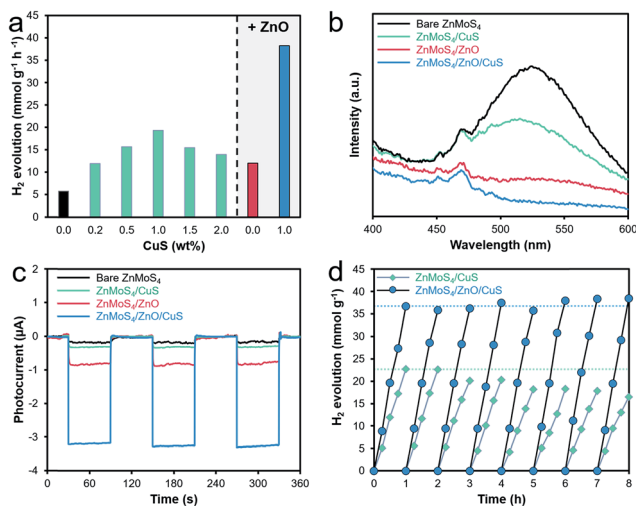


Fig. 5 (a) Photocatalytic hydrogen evolution rate of ZnMoS₄ with various CuS loading amounts and ZnO intercalated layers in 0.25 M/0.35 M Na₂S/Na₂SO₃ aqueous solution with UV LED illumination. (b) Photoluminescence under 325 nm wavelength photon excitation and (c) photoelectrochemical measurements, obtained by switching between dark and UV LED illumination conditions every one minute. (d) Photocatalytic hydrogen evolution stability test for 8 h, repurged with Argon gas at every hour mark.

presented at the right end of Fig. 5a. It is shown that the surface modification of ZnMoS₄ with a ZnO interface could generate H₂ at a rate of 12.05 mmol g⁻¹ h⁻¹, or a 108% enhancement in performance. It is believed that this considerable photocatalytic enhancement can be attributed to the high porosity that allows the formation of favorable ZnO interfaces within the ZnMoS₄ hexagonal plate microstructure. Progressively, by loading 1 wt% CuS on top of ZnMoS₄/ZnO, the photocatalytic hydrogen evolution rate rose to as high as 38.22 mmol g⁻¹ h⁻¹, corresponding to 560% and 217% enhancement in performance compared to bare ZnMoS₄ and ZnMoS₄/ZnO, respectively. Putting this result into another context, the presence of a ZnO intercalated layer in ZnMoS₄/ZnO/CuS asserts a 97% improvement in photocatalytic performance, in comparison to ZnMoS₄/CuS (19.38 to 38.22 mmol g⁻¹ h⁻¹), substantiating the positive effect of this intercalated layer in the photocatalyst heterojunction in further promoting the photocatalytic activity.

UV-vis spectra and Tauc plots were scanned and derived for all photocatalysts, as shown in Fig. S5.† All ZnMoS₄ composites show a lower band gap than the bare ZnMoS₄ (3.35 eV). Band gaps of 3.24 eV, 3.18 eV and 3.12 eV are determined for ZnMoS₄/CuS, ZnMoS₄/ZnO and ZnMoS₄/ZnO/CuS, respectively. It is observed that ZnO induces a slight red-shift in the band edge while CuS enhances the overall absorbance in the visible light range. Both features are expected to enhance light absorption abilities and consequently increase the photo-generation of electron-hole pairs, justifying the higher photoactivity of ZnMoS₄/ZnO/CuS. Beyond that, the effect on charge carrier dynamics associated with multi-interfacial heterostructures was investigated using photoluminescence (PL) emission spectra and photoelectrochemical (PEC) measurements. From Fig. 5b, it is observed that bare ZnMoS₄ generates high PL intensity,

specifically at about 530 nm, indicating a high recombination of photo-excited electron-hole pairs within the photocatalyst. The possible origin of this emission band at 530 nm is the sulfur species on the surface.^{46,47} This high surface recombination characteristic brings about adverse photocatalytic activity as the photo-generated charge carriers were largely consumed by recombination rather than the water reduction reaction. Therefore, surface modification with ZnO becomes crucial. As observed from the PL spectra in Fig. 5b, the presence of either the ZnO or the CuS interface decreases the PL intensity, indicating a reduced recombination. However, it is noticed that the ZnO interface exhibits a higher suppression of surface recombination. The hypothesis is that CuS predominantly enhances the surface charge transfer through heterojunction formation while it is less effective in reducing the generic surface recombination, indicated by the noticeably high PL peak intensity at 530 nm. On the other hand, with the ZnO formation *via* thermal annealing, the sulfur surface recombination sites were effectively eliminated through surface composition reconstruction. This result clearly shows the critical role of ZnO in uncovering the full potential of ZnMoS₄ for photocatalysis. Collectively, by successive formation of heterojunctions, ZnMoS₄/ZnO/CuS exhibits a synergistic reduction in recombination, as reflected in its PL spectrum, quenching the 530 nm PL peak to its minimal. Moreover, electrical impedance spectra in Fig. S6a† confirm the enhanced charge transfer in ZnMoS₄/ZnO/CuS induced by the ZnO intercalation in the ZnMoS₄/CuS heterojunction, from its smaller charge transfer radius (impedance R_{ct}).³² Besides that, Mott-Schottky plots in Fig. S6b† not only display a 100 meV flat band potential shift to a higher cathodic shift ascribed to CuS loading, typical of p-n junction formation according to the literature,^{48,49} but also show a higher carrier density or lower charge recombination (gentler M-S slope) of ZnMoS₄/ZnO/CuS resulted from the ZnO intercalation.⁵⁰ This illustrates that, as compared to those photocatalysts that consist of a single interface, the dual heterojunction interfaces of ZnMoS₄/ZnO/CuS effectively prohibit the occurrence of sulfur species surface recombination and enhance the charge transfer process simultaneously, thus establishing an efficient utilization of photo-excited charge carriers toward the water reduction reaction. Furthermore, besides evaluating surface recombination, photoelectrochemical measurements were used to assess the photo-generated charge carrier separation dynamics towards electrochemical reactions, particularly as a photocathode for the hydrogen evolution reaction under light illumination.⁵¹⁻⁵⁴ A photocathodic response upon light illumination can be observed in all photocatalyst electrodes, illustrating their function in the photo-activated hydrogen evolution electrochemical reaction. Their photocurrent magnitudes are depicted as follows: ZnMoS₄ < ZnMoS₄/CuS < ZnMoS₄/ZnO < ZnMoS₄/ZnO/CuS. Correspondingly, it is demonstrated that ZnO/CuS dual interfaces provide the most efficient charge separation process. This result agrees with the PL spectra and thus strongly suggests the inhibition of surface recombination of ZnMoS₄ with the presence of the ZnO/CuS dual interface as the key avenue for efficient interfacial charge transfer.

It is known that sulfide photocatalysts are susceptible to photocorrosion, or oxidation of sulfide, and lead to oxidative degradation of photocatalysts.^{14,55,56} Hence, to ensure sulfide photocatalyst stability in the water reduction process, it must be protected from oxidation. The oxidation of sulfur involves photo-generated holes and other active species, especially hydroxyl radicals ($\cdot\text{OH}$).⁵⁷ It is noted that even though photo-generated holes in photocatalytic reactions are inevitable, effective shielding of the photocatalyst from other reactants can possibly eliminate photocorrosion issues. As metal oxides are fairly more resistant to oxidation than sulfides,⁵⁷ a ZnO passivated sulfide surface will have adequate photocorrosion resistance. An eight-hour-long photocatalytic hydrogen evolution experiment was conducted to monitor the stability of the photocatalyst with and without the ZnO intercalated layer. It appears that the ZnO intercalated layer offers not only an enhancement in performance due to the aforementioned reasons, but also an improved photocatalytic stability (Fig. 5d). Negligible degradation in photocatalytic performance was detected with $36.69 \text{ mmol g}^{-1}$ at the first hour mark to $38.46 \text{ mmol g}^{-1}$ of hydrogen detected at the eighth hour mark. On the other hand, without the ZnO layer, the photocatalytic performance decreased almost every 2 hours. The hydrogen evolution yield decreased from $22.69 \text{ mmol g}^{-1}$ at the first hour mark to $16.40 \text{ mmol g}^{-1}$ at the eighth hour mark, equivalent to a 27.72% deterioration over 8 hours. SEM and XRD data were obtained from the $\text{ZnMoS}_4/\text{CuS}$ and $\text{ZnMoS}_4/\text{ZnO}/\text{CuS}$ photocatalysts after the stability tests, as shown in Fig. S7.† Although both the samples fairly preserve the hexagonal plate morphologies, the dominant ZnMoS_4 peak intensity of the $\text{ZnMoS}_4/\text{CuS}$ sample is seen to decrease, whereas for the $\text{ZnMoS}_4/\text{ZnO}/\text{CuS}$ sample all the diffraction peak intensities are well retained. This may suggest the ability of ZnO to inhibit the photocorrosion of ZnMoS_4 to a certain extent. Moreover, with reference to the recent literature,⁵⁸ photocatalytic H_2 evolution measurements should be performed in pure water to demonstrate the real water splitting abilities, as they are usually obscured by sacrificial agent induced hydrogen evolution through an indirect oxidation path,⁵⁹ and especially in this case of $\text{Na}_2\text{S}/\text{Na}_2\text{SO}_3$, SH^- is oxidized to S and H_2 . Fig. S8† shows that all ZnMoS_4 , $\text{ZnMoS}_4/\text{CuS}$, $\text{ZnMoS}_4/\text{ZnO}$ and $\text{ZnMoS}_4/\text{ZnO}/\text{CuS}$ are able to perform photocatalytic hydrogen evolution at rates of 0.12, 0.51, 0.24 and $1.19 \text{ mmol g}^{-1} \text{ h}^{-1}$, respectively, in pure water. The H_2 evolution rate for the pure water is 32- to 50-fold lower than those for the $\text{Na}_2\text{S}/\text{Na}_2\text{SO}_3$ sacrificial agent. Importantly, the photoactivity trend of $\text{Na}_2\text{S}/\text{Na}_2\text{SO}_3$ aqueous solution is the same as those of pure water splitting without the sacrificial agent.

Numerous studies were referred to analyse their Fermi level and band alignment and to ultimately understand their mechanism in generating an efficient photocatalytic hydrogen evolution reaction.^{43,60–66} The simplified band structures of $\text{ZnMoS}_4/\text{CuS}$ and $\text{ZnMoS}_4/\text{ZnO}/\text{CuS}$ in this report are illustrated in Fig. 6. Notably, the narrower band gap in ZnMoS_4 , caused by the incorporation of Mo species provides additional photo-generated electrons upon light excitation with energy larger than its band gap energy of 3.35 eV or a photon

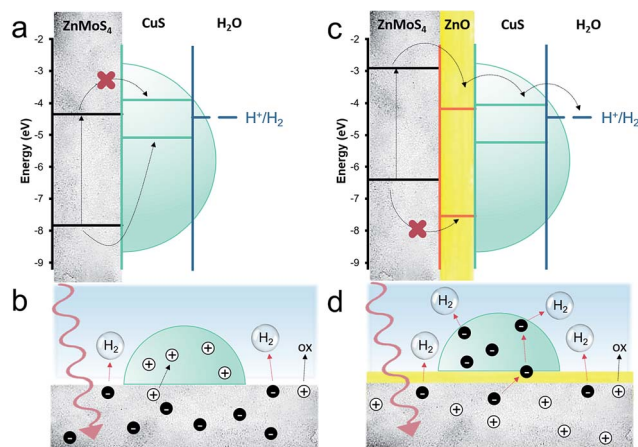


Fig. 6 Electronic band alignments relative to water redox potentials and possible transfer routes of electrons and holes and the corresponding schematic illustrations of charge carrier and active species dynamics of (a and b) $\text{ZnMoS}_4/\text{CuS}$ and (c and d) $\text{ZnMoS}_4/\text{ZnO}/\text{CuS}$, respectively.

wavelength larger than 370 nm. ZnMoS_4 and CuS form a p-n heterojunction and their band positions are shown in Fig. 6a. From the band diagram, CuS promotes the photo-generated charge separation of ZnMoS_4 , as proven by PL and PEC results, by sweeping holes into the CuS interface while retaining electrons within ZnMoS_4 . Hence, there is minimal water reduction reaction occurring at the CuS sites. The photocatalytic hydrogen evolution is restricted to the ZnMoS_4 surface that is not covered by the CuS cocatalyst where the electrons can interact with water, as depicted in Fig. 6b. Clearly, even though the photocatalytic performance is enhanced by the CuS heterojunction through charge separation, the photocatalytic charge dynamics between the heterostructure and water is not optimized. On the other hand, the type II heterojunction configuration of $\text{ZnMoS}_4/\text{ZnO}$ induces photo-generated holes to be mostly trapped in ZnMoS_4 , while electrons are transported to ZnO , thus achieving outstanding photo-generated charge carrier separation, as demonstrated in Fig. 6c. More importantly, the formation of the ZnO layer induces an interfacial band bending on ZnMoS_4 , which particularly lowers the ZnMoS_4 Fermi level to the level close to that of CuS . Hence when CuS subsequently comes into contact to form a second heterojunction, the overall band level shift becomes less abrupt. In addition, as ZnO significantly suppresses charge carrier recombination, based on the PL emission spectra in Fig. 5b, the electron diffusion length is crucially extended and favours the electron transport across its nanoscale thickness.^{67,68} In other words, the ZnO intercalated layer plays a crucial role in maintaining the thermodynamic driving force for photo-generated electrons to be transported from ZnMoS_4 to CuS surfaces. Unlike the typical p-n heterojunction present in $\text{ZnMoS}_4/\text{CuS}$, the photogenerated electrons for the $\text{ZnMoS}_4/\text{ZnO}/\text{CuS}$ ternary configuration are efficient in migrating to both the ZnO and CuS surfaces to effectively reduce water for hydrogen evolution, as depicted in Fig. 6d.

Conclusions

In summary, a novel ternary chalcogenide photocatalyst ZnMoS₄ with a 2D hexagonal plate has been developed through sulfidation from its oxide form Zn₅Mo₂O₁₁, acting as a chemical source and a 2D microstructure template. The ZnMoS₄ exhibits an enhancement in intrinsic carrier density and interfacial charge transfer with the electrolyte, as well as an increase in light absorption from its narrow band gap originated from its Mo species. Consequently, the photocatalytic hydrogen properties of ZnMoS₄ have been tested and it demonstrated an almost 3-fold higher photocatalytic hydrogen generation rate as compared to ZnS. To further exploit its potential, a ZnO layer is introduced into the p–n heterostructure, prior to the formation of CuS. Besides suppressing the surface recombination of ZnMoS₄ and promoting the electron transfer through the type II heterojunction configuration of ZnMoS₄, it has been found that the ZnO interface in the ZnMoS₄/ZnO/CuS multi-junction heterostructures induces desirable electron migration towards photocatalyst surfaces. With the optimized electron transfer dynamics for photocatalytic hydrogen evolution, high efficiency of photocatalytic activity has been demonstrated, resulting in a 97% and a 560% improvement in the generation rate, as compared to ZnMoS₄/CuS and bare ZnMoS₄. Essentially, this work provides a new insight into band structure engineering in heterostructure design for efficient charge carrier dynamics and electrochemical reactivity.

Conflicts of interest

There are no conflicts to declare.

Acknowledgements

This research is supported by the Ministry of Education (MOE), Singapore under MOE grants R-263-000-C85-112 and R-263-000-D08-114.

Notes and references

- B. Han and Y. H. Hu, *Energy Sci. Eng.*, 2016, **4**, 285–304.
- G.-J. Lee and J. J. Wu, *Powder Technol.*, 2014, **318**, 8–22.
- B. Zhu, B. Lin, Y. Zhou, P. Sun, Q. Yao, Y. Chen and B. Gao, *J. Mater. Chem. A*, 2014, **2**, 3819.
- M. Dong, P. Zhou, C. Jiang, B. Cheng and J. Yu, *Chem. Phys. Lett.*, 2017, **668**, 1–6.
- A. Kudo and M. Sekizawa, *Chem. Commun.*, 2000, 1371–1372.
- J. W. Jang, S. H. Choi, J. S. Jang, J. S. Lee, S. Cho and K.-H. Lee, *J. Phys. Chem. C*, 2009, **113**, 20445–20451.
- I. Tsuji, H. Kato and A. Kudo, *Chem. Mater.*, 2006, **18**, 1969–1975.
- T. Torimoto, Y. Kamiya, T. Kameyama, H. Nishi, T. Uematsu, S. Kuwabata and T. Shibayama, *ACS Appl. Mater. Interfaces*, 2016, **8**, 27151–27161.
- Y. Li, J. Wang, S. Peng, G. Lu and S. Li, *Int. J. Hydrogen Energy*, 2010, **35**, 7116–7126.
- A. Wu, L. Jing, L. Wang, Y. Qu, Y. Xie, B. Jiang, C. Tian and H. Fu, *Sci. Rep.*, 2015, **5**, 8858.
- Z. Wang, S.-W. Cao, S. C. J. Loo and C. Xue, *CrystEngComm*, 2013, **15**, 5688–5693.
- C. Mondal, A. Singh, R. Sahoo, A. K. Sasmal, Y. Negishi and T. Pal, *New J. Chem.*, 2015, **39**, 5628–5635.
- W. J. Kin, E. Jang and T. J. Park, *Appl. Surf. Sci.*, 2017, **419**, 159–164.
- P. Weide, K. Schulz, S. Kaluza, M. Rohe, R. Beranek and M. Muhler, *Langmuir*, 2016, **32**, 12641–12649.
- L. Yu, W. Chen, D. Li, J. Wang, Y. Shao, M. He, P. Wang and X. Zheng, *Appl. Catal., B*, 2015, **164**, 453–461.
- F.-X. Xiao, J. Miao and B. Liu, *J. Am. Chem. Soc.*, 2014, **136**, 1559–1569.
- W. Yin, L. Bai, Y. Zhu, S. Zhong, L. Zhao, Z. Li and S. Bai, *ACS Appl. Mater. Interfaces*, 2016, **8**, 23133–23142.
- M. Wang, Y. Hu, J. Han, R. Guo, H. Xiong and Y. Yin, *J. Mater. Chem. A*, 2015, **3**, 20727–20735.
- J. Zhang, S. Z. Qiao, L. Qi and J. Yu, *Phys. Chem. Chem. Phys.*, 2013, **15**, 12088–12094.
- H. B. Ahn and J. Y. Lee, *CrystEngComm*, 2013, **15**, 6709–6714.
- Y. Tang, T. Chen, S. Yu, Y. Qiao, S. Mu, J. Hu and F. Gao, *J. Mater. Chem. A*, 2015, **3**, 12913.
- J. S. Cho, J.-S. Park and Y. C. Kang, *Nano Res.*, 2017, **10**, 897–907.
- S. Sun, D. Deng, X. Song and Z. Yang, *Phys. Chem. Chem. Phys.*, 2013, **15**, 15964.
- S. H. Mohamed, M. E. Hagary and M. E. Ismail, *J. Phys. D: Appl. Phys.*, 2010, **43**, 075401.
- S. Park, C. Jin, H. Kim, C. Hong and C. Lee, *J. Lumin.*, 2012, **132**, 231–235.
- A. K. Kole, C. S. Tiwary and P. Kumbhakar, *J. Mater. Chem. C*, 2014, **2**, 4338.
- V. S. Perera, N. P. Wickramaratne, M. Jaroniec and S. D. Huang, *J. Mater. Chem. B*, 2014, **2**, 257–261.
- G. H. Guo, Y. T. Tao, Z. P. Song and K. L. Zhang, *J. Solid State Electrochem.*, 2007, **11**, 90–92.
- I. Shakir, M. Shahid and D. J. Kang, *Chem. Commun.*, 2010, 46, 4324–4326.
- L. Wan, J. Shen, Y. Zhang and X. Li, *J. Alloys Compd.*, 2017, **708**, 713–721.
- C. Xiao, Y. Li, X. Lu and C. Zhao, *Adv. Funct. Mater.*, 2016, **26**, 3515–3523.
- W. Y. Lim, Y.-F. Lim and G. W. Ho, *J. Mater. Chem. A*, 2017, **5**, 919–924.
- G. Li, J. Sun, W. Hou, S. Jiang, Y. Huang and J. Geng, *Nat. Commun.*, 2016, **7**, 10601.
- Y. Son, J.-S. Lee, Y. Son, J.-H. Jang and J. Cho, *Adv. Energy Mater.*, 2015, **5**, 1500110.
- W. Y. Lim, M. Hong and G. W. Ho, *Dalton Trans.*, 2016, 552.
- M. Luo, W. Yao, C. Huang, Q. Wu and Q. Xu, *J. Mater. Chem. A*, 2015, **3**, 13884.
- G. H. Huo, Y. T. Tao, Z. P. Song and K. L. Zhang, *J. Solid State Electrochem.*, 2007, **11**, 90–92.
- V. S. Perera, N. P. Nickramaratne, M. Jaroniec and S. D. Huang, *J. Mater. Chem. B*, 2014, **2**, 257–261.

- 39 Z. Hu, M. Xu, Z. Shen and J. C. Yu, *J. Mater. Chem. A*, 2015, **3**, 14046.
- 40 W. Li, P. Da, Y. Zhang, Y. Wang, X. Lin, X. Gong and G. Zheng, *ACS Nano*, 2014, **8**, 11770–11777.
- 41 M. Ye, J. Gong, C. Lin and Z. Lin, *J. Am. Chem. Soc.*, 2012, **134**, 15720–15723.
- 42 W. Feng, Z. Fang, B. Wang, L. Zhang, Y. Zhang, Y. Yang, M. Huang, S. Weng and P. Liu, *J. Mater. Chem. A*, 2017, **5**, 1387.
- 43 O. Ola and M. M. M. Valer, *J. Photochem. Photobiol., C*, 2015, **24**, 16–42.
- 44 U. P. Gawai, U. P. Deshpande and B. N. Dole, *RSC Adv.*, 2017, **7**, 12382.
- 45 J. Wang, Y.-F. Lim and G. W. Ho, *Nanoscale*, 2014, **6**, 9673–9680.
- 46 C. Lan, J. Gong, Y. Jiang and Q. Ding, *CrystEngComm*, 2012, **14**, 8063–8067.
- 47 J. Schneider and D. W. Bahnemann, *J. Phys. Chem. Lett.*, 2013, **4**, 3479–3483.
- 48 B. Mukherjee, A. Peterson and V. Subramanian, *Chem. Commun.*, 2012, **48**, 2415–2417.
- 49 E. Aguilera-Ruiz, M. de la Garza-Galván, P. Zambrano-Robledo, J. C. Ballesteros-Pacheco, J. Vazquez-Arenas, J. Peraldi and U. M. García-Pérez, *RSC Adv.*, 2017, 45885–45895.
- 50 N. Bhandary, A. P. Singh, P. P. Ingole and S. Basu, *RSC Adv.*, 2016, **6**, 35239–35247.
- 51 J. Liu, T. Hisatomi, D. H. K. Murthy, M. Zhong, M. Nakabayashi, T. Higashi, Y. Suzuki, H. Matsuzaki, K. Seki, A. Furube, N. Shibata, M. Katayama, T. Minegishi and K. Domen, *J. Phys. Chem. Lett.*, 2017, **8**, 375–379.
- 52 S. P. Berglund, F. F. Abdi, P. Bogdanoff, A. Chemseddine, D. Friedrich and R. van de Krol, *Chem. Mater.*, 2016, **28**, 4231–4242.
- 53 H. Qi, J. Wolfe, D. Fichou and Z. Chen, *Sci. Rep.*, 2016, **6**, 30882.
- 54 X. Lu and Z. Liu, *Dalton Trans.*, 2017, **46**, 7351.
- 55 Y. Tang, X. Hu and C. Liu, *Phys. Chem. Chem. Phys.*, 2014, **16**, 25321.
- 56 J. Xian, D. Li, J. Chen, X. Li, M. He, Y. Shao, L. Yu and J. Fang, *ACS Appl. Mater. Interfaces*, 2014, **6**, 13157–13166.
- 57 S. Chen and L.-W. Wang, *Chem. Mater.*, 2012, **24**, 3659–3666.
- 58 P. V. Kamat and S. Jin, *ACS Energy Lett.*, 2018, **3**, 622–623.
- 59 G. Shen, Y. Bando and D. Golberg, *Appl. Phys. Lett.*, 2006, **88**, 123107.
- 60 J. Heo, G.-H. Kim, J. Jeong, Y. J. Yoon, J. H. Sea, B. Walker and J. Y. Kim, *Sci. Rep.*, 2016, **6**, 36608.
- 61 S.-K. Han, C. Gu, S. Zhao, S. Xu, M. Gong, Z. Li and S.-H. Yu, *J. Am. Chem. Soc.*, 2016, **138**, 12913–12919.
- 62 G. Wang, Z. Li, M. Li, C. Chen, S. Lv and J. Liao, *Sci. Rep.*, 2016, **6**, 29470.
- 63 J. Sun, M. Ikezawa, X. Wang, P. Jing, H. Li, J. Zhao and Y. Masumoto, *Phys. Chem. Chem. Phys.*, 2015, **17**, 11981.
- 64 S. K. Goswami, J. Kim, K. Hong, E. Oh, Y. Yang and D. Yu, *Mater. Lett.*, 2014, **133**, 132–134.
- 65 S. Berardi, S. Drouet, L. Francas, C. G. Surinach, M. Gettentag, C. Richmond, T. Stoll and A. Llobet, *Chem. Soc. Rev.*, 2014, **43**, 7501–7519.
- 66 J. Liu, C. Gao, L. Luo, Q. Ye, X. He, L. Ouyang, X. Guo, D. Zhuang, C. Liao, J. Mei and W. Lau, *J. Mater. Chem. A*, 2015, **3**, 11750.
- 67 J. P. Gonzalez-Vazquez, J. A. Anta and J. Bisquert, *J. Phys. Chem. C*, 2010, **114**, 8552–8558.
- 68 A. G. Vega-Poot, M. Macías-Montero, J. Idígoras, A. Borrás, A. Barranco, A. R. Gonzalez-Elipé, F. I. Lizama-Tzec, G. Oskam and J. A. Anta, *ChemPhysChem*, 2014, **15**, 1088–1097.